Properties of nanostructured hematite prepared by various coating techniques for potential PEC water splitting applications

Adiel Holtzhausen, Justine S Nyarige, Pannan I Kyesmen, Mmantsae Diale*

Department of Physics, University of Pretoria, Private Bag X20, Hatfield 0028, South Africa

Corresponding author's e-mail addresses: mmantsae.diale@up.ac.za

Abstract

In this study, hematite (α-Fe_2O_3) thin films were synthesized using dip coating and spray pyrolysis techniques on fluorine-doped tin oxide substrates, and the morphological, optical, and structural properties of the hematite were studied. Six peaks were identified for both techniques from X-ray diffraction measurements. The (104) and (110) phases which are the main peaks describe the corundum structure of α-Fe_2O_3 while other peaks further confirm the formation of high purity α-Fe_2O_3. Raman spectroscopy revealed seven vibrational modes (two A_{1g} and five E_g modes) of α-Fe_2O_3 were observed within the first Brillouin zone. Field emission scanning electron microscopy revealed mesoporous hematite nanospheres. The grain sizes were determined by average grain intercept and estimated as 45.8±0.5 and 50.0±0.5 nm respectively for films prepared by spray pyrolysis and dip-coating. Ultraviolet-visible spectroscopy results showed good absorbance for both techniques with the absorbance onset at 597 nm for dip coated films as compared to onset at 609 nm for spray pyrolysis films. From this work it was determined that coating techniques can affect the grain sizes of hematite films. This could potentially contribute to improved absorption of light for photoelectrochemical water splitting applications.

Keywords: hematite nanostructures, dip-coating, spray pyrolysis, structural properties, optical properties

1. Introduction

Photoelectrochemical (PEC) water splitting, as a means of energy production, has been a topic of great research interest. Fujishima and Honda who were the first to report a successful PEC experiment in 1972 using titanium dioxide (TiO_2) as a photoanode for PEC water splitting realized low efficiencies [1]. The idea of using TiO_2 provided some challenges due to its fast electron-hole recombination rates, along with a large bandgap of 3.2 eV which absorbs in the ultraviolet region of the electromagnetic spectrum. Since then, other semiconductors have been explored as possible photoanodes. Some of these semiconductors include zinc oxide (ZnO) [2], tantalum oxynitride (TaON) [3], tungsten trioxide (WO_3) [4], bismuth vanadate ($BiVO_4$) [5], cadmium selenide (CdSe) [6] and hematite (α-Fe_2O_3) [7-9]. Among these, hematite is favourable since it is the most abundant metal oxide semiconductor, it is also non-toxic, and stable in ionic solutions [10]. In addition, hematite absorbs 40 % of visible light due to its low bandgap that ranges from 1.9 to 2.2 eV [9, 11, 12]. However, there are some associated limitations such as low conductivity, low charge separation efficiency, and high electron-hole recombination rate leading to short excitation lifetimes of 3-10 ps [12, 13]. Possible solutions to these limitations include the use of over and under layers of metal oxides such as zirconium dioxide (ZrO_2) [14] and titanium dioxide (TiO_2) [15], doping, nanostructuring and anodization

[16-18]. In addition, nanostructures such as nanorods [19], nanoflowers [20], nanospheres [21], nanotubes [22], nanowires [23] and nanosheets [24]; have been reported to influence the optical, structural and photoelectrical properties [25, 26]. Tamirat *et al.* reported that nanostructures with small diameters increased charge mobility by minimizing hole diffusion lengths at the semiconductor-electrolyte interface [12]. However, Phuan *et al.* reported that nanoparticles such as nanotubes, nanorods, nanoporous, and nanohoneycombs demonstrate large surface areas which led to improved PEC performance [27]. Whereas Kyesmen *et al.* reported that hematite nanostructures prepared by dip coating, showed better absorption in the visible region when compared to those of spin coating and combined coating techniques [8]. Thus, comparative studies are imperative as there has not yet been much research in comparing coating techniques.

Various preparation techniques such as dip coating, spray-pyrolysis, spin coating, electrodeposition, and microemulsion-precipitation for preparing nanostructured hematite films have been reported [8, 16]. Amidst these, spray pyrolysis and dip coating are some of the most effortless methods due to the simplicity of colloidal solution-based techniques [8, 9, 28]. This technique entails coating a porogen and a dispersion of particles onto a conducting substrate, the film is then dried and annealed in oxygen or air which leaves porous interconnected nanoparticles [8, 13].

Dip coating is a commonly used cost-efficient method for synthesizing hematite thin films, suitable for PEC water splitting [29, 30]. Dip coating is a process by which a cleaned substrate is slowly lowered into a precursor solution and then withdrawn at a constant rate, to form a thin coating on the substrate. The nanoparticle sizing for dip coating can be influenced by viscous drag, gravity, surface tension, and inertial forces. Thus, any disturbance in atmospheric conditions can influence the coating as the sample is withdrawn. This could lead to surface defects such as craters and dots due to external particles landing on the wet substrate [8]. Spray pyrolysis is less cost-efficient but, has the potential to create a variation in nanoparticles. It is the process in which a precursor solution is sprayed, from a fixed height, at a constant spray rate onto a heated, cleaned substrate and left to dry. This forms a thin film coating on top of the substrate which is made up of nanoparticles. The nanoparticles for spray pyrolysis can be influenced by spray pressure and the deposition temperature. At temperatures above 300 °C, the deposition takes place in the form of vapour thus producing nanostructured grains distributed evenly on the substrate, whereas at low heating temperatures, the deposition takes place in liquid form where most of the precursors land on the substrate. [31].

In this study, nanostructured hematite thin films were prepared by spray-pyrolysis and dip coating. Nanospheres along with agglomerated nanodisks, nanolarvae and nanospheres were obtained from the two deposition techniques. Both techniques produced different grain sizes ranging from ~ 45 – 50 nm which could potentially influence absorption. Dip coating typically yields nanospheric particles whereas spray pyrolysis can yield nanospheres, nanocones, nanodisks or nanotubes [12]. Both dip coating and spray pyrolysis are commonly used in the synthesis of hematite thin films. Thus, more studies into how different coating techniques affect grain sizes and nanostructuring affects absorption could be beneficial for applications in PEC water splitting.

2. Experimental

Hematite nanoparticles were produced from ferrous iron(III)nitrate nonahydrate ($Fe(NO_3)_3.9H_2O$) and deionized water (H_20). These two compounds reacted to form iron

oxyhydrate ($Fe(OH)_3$), which was annealed for 1 h at 500 °C to dissipate the excess water which forms α-Fe_2O_3.

The reaction is described by the following equations [12]:

$$3Fe(NO_3)_3.9H_2O \rightarrow 3Fe^{3+} + 9NO_3^- + 9H_2O \quad (1)$$

$$Fe^{3+} + 3OH^- \rightarrow Fe(OH)_3 \quad (2)$$

$$2Fe(OH)_3 + 3H_2O \xrightarrow{heat} \alpha - Fe_2O_3 + 6H_2O \quad (3)$$

2.1.Substrate cleaning

Fluorine-doped tin oxide (FTO) substrates were cleaned by rinsing in deionized water (DI), next they were placed in an ultrasonic bath with acetone, followed by ethanol for 15 min each. This was followed by one more rinse with deionized water and lastly blown dry with nitrogen gas [33].

2.2. Synthesis of hematite nanostructures

2.2.1. Dip-coating

The precursor solution was prepared by mixing a 2:1 mol ratio of iron(III)nitrate nonahydrate ($Fe(NO_3)_3.9H_2O$, AR, 99%, Sigma Aldrich, Sigma Aldrich, Johannesburg, South Africa) and oleic acid ($C_{18}H_{34}O_2$, GC, 99%, Sigma Aldrich, Johannesburg, South Africa); then heated at 110 °C for 2.5 h, forming a brick red mass of iron oleate ($C_{36}H_{66}FeO_4$). The iron oleate ($C_{36}H_{66}FeO_4$) solution obtained was treated with tetrahydrofuran ($(CH_2)_4O$) and sonicated for 10 min, and finally centrifuged for 3 min at 5000 rpm. The supernatant solution was collected as a precursor solution for dip coating. The cleaned FTO substrates were dipped into the precursor solution and left for 2 min, after which, withdrawn at a 30 mm/min rate; then left to dry for 15 min on a hotplate at 70 °C. The samples were annealed at 500 °C for 1 h, to form α-Fe_2O_3 phase. The procedure was repeated four times to produce four layers of α-Fe_2O_3 thin film.

2.2.2.Spray pyrolysis

The precursor solution was synthesized by dissolving 50 mM of iron(III)nitrate nonahydrate ($Fe(NO_3)_3.9H_2O$, AR, 99%, Sigma Aldrich, Johannesburg, South Africa) into 200 ml of deionized (DI) water; then sprayed onto a heated FTO substrate. The FTO substrate was heated to 400 °C using a hotplate. The nozzle diameter of 1 mm with a spray rate of 10 ml per min were used. The substrate to nozzle distance (deposition height) of 20 cm was used. The temperature was measured by a resistor thermocouple while the flow rate and a spray pressure of 2.2 x 10^5 Pa was kept constant. Furthermore, the spray time was kept at 30 s. After four layers of spray pyrolysis, the samples were annealed at 500 °C for 1 h, forming four layers of α-Fe_2O_3 thin film.

2.3. Characterization

X-ray diffraction (XRD) measurements were performed by using a Bruker D2 PHASER X-ray diffractometer containing CuK_α radiation, with a 0.15418 nm source and scanning speed of

0.05° per minute in the *2θ* range of 20° and 80°, to study the crystal structure of the thin films. Raman spectroscopy measurements were performed using a WiTec alpha300 RAS+ confocal Raman microscope with a 532 nm excitation laser which performs at a power of 5 mW. The surface morphology of the thin films was investigated with a Zeiss Gemini Ultra Plus 55 field emission scanning microscope (FE-SEM). Absorption and transmittance measurements were performed using a CARY 100 Bio UV-Vis spectrometer.

3. Results and discussion

3.1. X-ray diffraction analysis

Figure 1 shows XRD measurements of hematite films. Six peaks were identified and indexed at: 24.33º for (012), 33.94º for (104), 35.90º for (110), 49.81º for (024), 54.55º for (122), and 61.82º for (124) for the spray pyrolysis thin film and at: 24.35º for (012), 33.83º for (104), 35.73º for (110), 49.50 º for (024), 54.57º for (122) and 61.57º for (124) for the dip-coated thin film. This correlates with the JCPDS 33-0664 plot card [34, 35].

The peak width indicates the size and state of the crystal structure. The narrow peaks indicate that the calcination of the crystal structure from ɣ- Fe_2O_3 (magnetite) to α-Fe_2O_3 (hematite) has taken place when the samples were annealed from 400 °C - 500 °C [36, 37]. This confirmed that the α-Fe_2O_3 nanostructures had high purity. The diffraction patterns at (104) and (110) present the rhombohedral structure of hematite denoted by the lattice constants of the trigonal-hexagonal unit cell a=b=0.5034 nm and c=1.375 nm; also denoted by a_{rh}=0.5427 nm and α=55.31° [35]. The more intense D-peaks from the dip coating samples are indicative of a thicker film, these two peaks confirm the corundum structure which is present in hematite. Both methods produced peaks within a range of 0.10° of one another, indicating a similarity in the crystal structure.

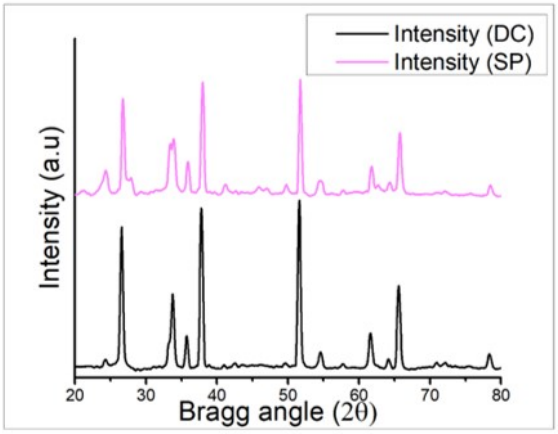

Fig. 1. XRD patterns of α-Fe_2O_3 films synthesized by (a) dip coating vs spray pyrolysis and (b) spray-pyrolysis and (c) dip coating.

The full width at half maximum measurements (FWHM) was calculated with the Origin Pro 9.1 software using the six peaks for hematite. The Debye-Scherrer formula (equation 4) was then used to estimate the crystallite sizes for each peak [38, 39]:

$$D = \frac{k\lambda}{d\cos\theta} \qquad 4$$

Where D denotes the crystallite size, k denotes the shape factor (0.9), λ denotes the x-ray wavelength (0.15418 nm), d denotes the full width at half maximum in radians and θ denotes the diffraction angle in radians.

The average crystal size for the dip coating thin film was 11.5 nm whereas the average for spray pyrolysis was 15.45 nm. Thus, the coating technique could have influenced the crystallite size of the hematite thin films. These crystal sizes were similar when compared to those found in Nyarige *et al.* [40].

Table 1. FWHM and crystal sizes for both dip coating (DC) and spray pyrolysis (SP).

Peak	FWHM DC (Degrees)	FWHM SP (Degrees)	2Theta DC (Degrees)	2Theta SP (Degrees)	D Crystal-size DC (nm)	D Crystal-size SP (nm)	Peak
012	0,98	0,97	24,29	24,34	8,34	8,37	012
104	0,56	0,42	33,78	33,93	14,78	19,81	104
110	0,49	0,53	35,76	35,91	16,98	15,71	110
024	2,10	0,62	49,67	49,77	4,30	14,08	024
112	1,01	0,46	57,69	51,75	9,02	19,42	112
214	0,59	0,60	61,60	61,80	15,58	15,34	214

3.2. Raman spectroscopy

Raman spectroscopy was performed, from which the crystallinity and structural information of the hematite thin films are presented in Figure 2. Seven vibrational phonon modes for hematite were found within the first Brillouin zone; two A_{1g} and five E_g modes confirmed with group theory [41, 42]. Both methods also yielded polycrystal nanostructures presented by strong vibrational modes of A_{1g} (230 cm^{-1}) and E_g (300 cm^{-1}) with high intensity. This confirms the purity of the hematite thin films as already presented by XRD. The longitudinal optical (LO) mode was present at around 650 cm^{-1} and the two-phonon scattering mode, (2LO), at 1305 cm^{-1} It was found that the 2LO mode had double the wavenumber of the LO mode, which confirms the magnetic properties of hematite. If this phenomenon does not occur, then an impurity of magnetite could be assumed. There was a red shift in the sample prepared by dip-coating as opposed to the one prepared by spray-pyrolysis, indicated by broadening of the E_g peaks, as a result of phonon-phonon scattering. The difference in intensity of peaks could be attributed to the frequency of annealing. The dip-coated samples had been annealed four times as opposed to the spray-pyrolysis sample which had been annealed once. The higher peak intensities of the

E_g modes could be indicative of improved crystallinity. This confirms the results obtained by XRD.

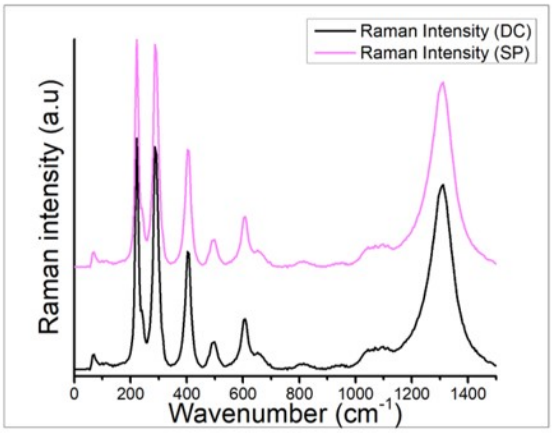

Fig. 2. Raman spectroscopy of α-Fe_2O_3 films for spray pyrolysis *vs.* dip coating.

3.3. Surface morphology

Field emission scanning electron microscopy (FE-SEM) was performed to study the surface morphology of the α-Fe_2O_3 thin films. From Figure 3, it is evident that both samples contained nanoparticles. From Figure 3b and 3d it could be concluded that the dip coating nanoparticles had a spherical and uniform appearance, whereas the spray-pyrolysis particles had shown some agglomeration of various shapes, including nanospheres, nanolarvae and nanodisks. The nanostructuring into spherical nanoparticles has been reported to improve photocurrent production. From Figures 3a and 3c it appeared that the spray-pyrolysis morphology was more homogeneous than the dip-coating thin film morphology. This is attributed to the even distribution during spraying when deposited, as well as the viscous drag of the dip coating solution. The grain size on the dip coating nanostructures was found to be larger than those of the spray-pyrolysis. Small homogeneous particles are favourable in PEC water splitting. The physical appearance of the films presented as an orange-brown colour, indicative of the absorption wavelength. It has been found that the orange-brown colour causes hematite to absorb up to 40 % of visible light. The grain size was determined with Average Grain Intercept (AGI) as 45.8±0.5 nm for the spray pyrolysis thin film as opposed to 50.0±0.5 nm for the dip-coated film.

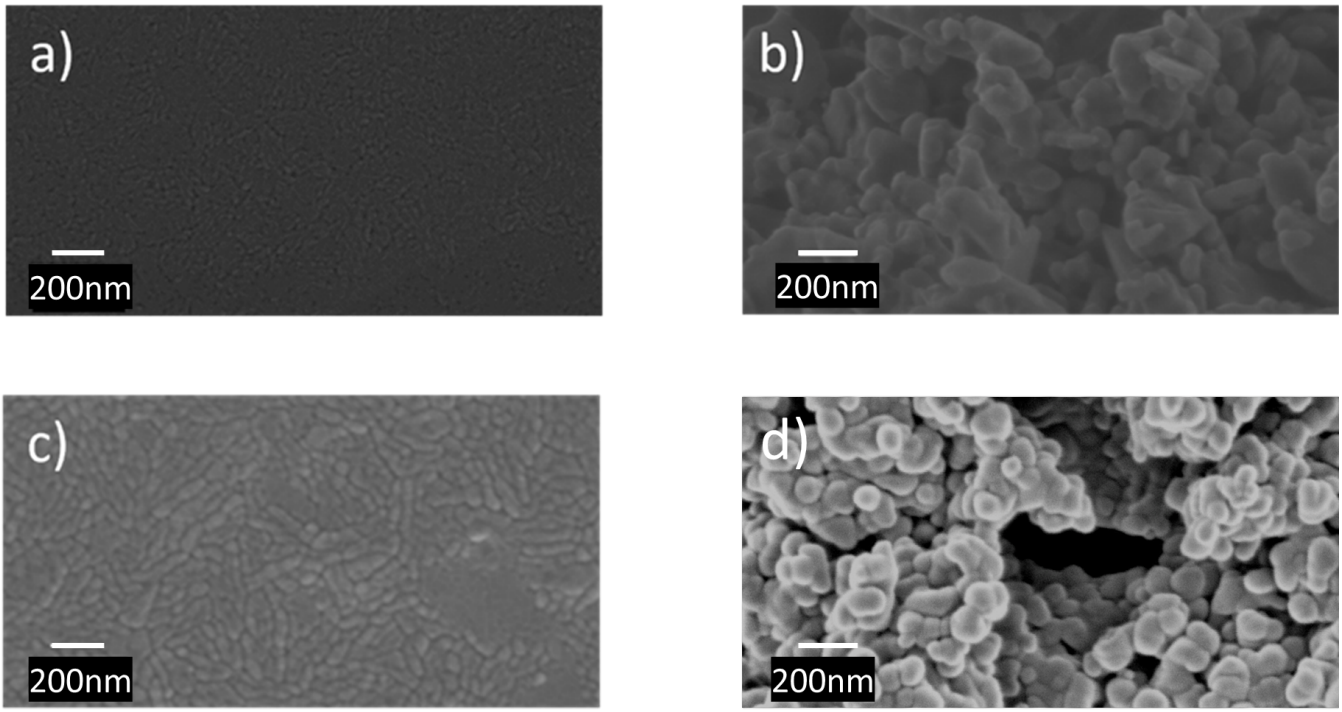

Fig. 3. FE-SEM images of α-Fe_2O_3 nanoparticles prepared by (a,b) spray-pyrolysis and (c,d) dip-coating.

3.4. Optical studies

Optical studies were performed on the hematite thin films by using ultraviolet-visible spectroscopy (UV-Vis) as shown in Figure 4. The absorbance of the sample prepared by spray pyrolysis was significantly more than those prepared by the dip coating. Both samples showed wavelength values of above 500 nm which indicated good absorption for hematite. In the visible spectrum, both samples showed similar absorption with maximum peaks of 442 nm and 448 nm respectively for dip coating and spray pyrolysis thin films. The lower absorbance of the dip coated film could partially be attributed to the smoother and glossier surface of the dip coated thin film, which could have led to surface reflection. The bandgap of both samples was estimated by Planck's Law:

$$E_g = h\nu \qquad 4$$

where E_g is the energy bandgap and $h\nu$ is the photon energy. The equation for ν is given by:

$$\nu = \frac{c}{\lambda} \qquad 5$$

where c is the speed of light and λ is the wavelength. These wavelengths were similar when compared to those found in Nyarige *et al.* using a Tauc plot [31, 40].

For dip coating the wavelength, as indicated by an arrow, was 597 nm which led to an estimated bandgap of 2.08 eV whereas spray pyrolysis had a wavelength of 609 nm, which led to a smaller estimated bandgap of 2.03 eV. From this it could be deduced that the spray pyrolysis sample was a better conductor as it had a smaller bandgap, thus electron flow was higher.

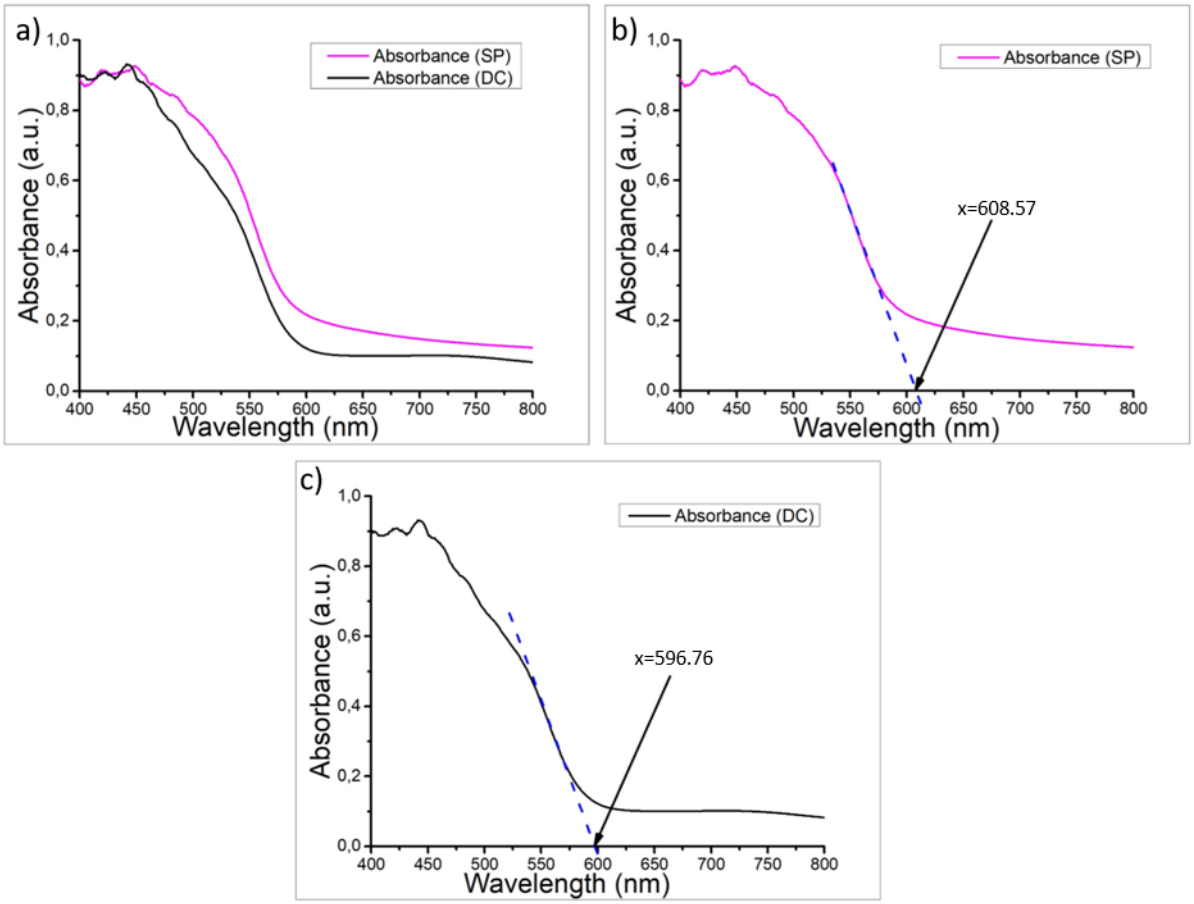

Fig. 4. Absorbance spectra of α-Fe_2O_3 films prepared by (a) spray pyrolysis *vs.* dip coating dip coating and (b) spray pyrolysis and (c) dip coating.

4. Conclusion

Spray-pyrolysis and dip coating methods were used to synthesize hematite thin films. The films were annealed at 500 °C for 1 h. FE-SEM analysis revealed agglomeration in the spray-pyrolysis film and spherical nanoparticles in the dip-coated film. Nanoparticles prepared by spray-pyrolysis (45.8±0.5 nm) were found to be smaller when compared to dip-coating (50.0±0.5 nm) and illustrated a homogeneous appearance. The particle grain sizes obtained from FE-SEM agreed with the values as found in literature. XRD studies confirmed that all samples followed the rhombohedral crystal structure for hematite, with all diffraction patterns present. Raman spectroscopy confirmed the results found from XRD, it also illustrated that thin films prepared by spray-pyrolysis might have a slight advantage in crystallinity. Optical studies performed by UV-Vis indicated that samples prepared by spray pyrolysis were more absorbent. The onset absorption ranged from 597 – 609 nm. This could be attributed to grain size as smaller grain size reduces grain boundaries which reduces the distance that light needs to travel in order to be absorbed. It was also noted that the spray pyrolysis (2.03 eV) samples had a smaller bandgap in comparison to dip-coating (2.08 eV) which is indicative of higher conductivity. This study suggests that the various nanoparticle production methods, as well as annealing frequency can influence the structural integrity of hematite thin films. Further studies in a broader range of techniques are recommended in order to make complete comparisons of all different coating techniques. Additionally, orthoferrites such as hematite which contains an optimal resonance

frequency (between 10 and 600 GHz) [43] and a low magnetic damping have recently been studied for advances in spin-wave research [44, 45]. Thus, further studies into the antiferromagnetic spin-wave dispersion of thin film hematite prepared by various coating techniques could potentially be useful in the development of hematite for use in advanced electric materials.

Acknowledgements

The authors would like to thank the Department of Physics, University of Pretoria for support, the National Research Foundation (NRF) grant No. N0115/115463 (SARChI, M.D.) and South African Research Chairs Initiative (SARChI), UID; 115463.

References

1. Fujishima, A. and K. Honda, *Electrochemical photolysis of water at a semiconductor electrode.* nature, 1972. **238**(5358): p. 37-38.
2. Luo, X., et al., *Enhanced photovoltaic response of the first polyoxometalate-modified zinc oxide photoanode for solar cell application.* Journal of Materials Chemistry, 2012. **22**(30): p. 15050-15055.
3. Higashi, M., K. Domen, and R. Abe, *Highly stable water splitting on oxynitride TaON photoanode system under visible light irradiation.* Journal of the American Chemical Society, 2012. **134**(16): p. 6968-6971.
4. Hodes, G., D. Cahen, and J. Manassen, *Tungsten trioxide as a photoanode for a photoelectrochemical cell (PEC).* Nature, 1976. **260**(5549): p. 312-313.
5. Toma, F.M., et al., *Mechanistic insights into chemical and photochemical transformations of bismuth vanadate photoanodes.* Nature communications, 2016. **7**(1): p. 1-11.
6. Ellis, A.B., S.W. Kaiser, and M.S. Wrighton, *Optical to electrical energy conversion. Characterization of cadmium sulfide and cadmium selenide based photoelectrochemical cells.* Journal of the American Chemical Society, 1976. **98**(22): p. 6855-6866.
7. Krishnakumar, R., et al., *Thin film preparation by spray pyrolysis for solar cells.* Materials chemistry and physics, 1987. **16**(5-6): p. 385-395.
8. Kyesmen, P.I., N. Nombona, and M. Diale, *Influence of coating techniques on the optical and structural properties of hematite thin films.* Surfaces and Interfaces, 2019. **17**: p. 100384.
9. Dias, P., et al., *Extremely stable bare hematite photoanode for solar water splitting.* Nano Energy, 2016. **23**: p. 70-79.
10. Kim, D.H., et al., *Vertically ordered hematite nanotube array as an ultrasensitive and rapid response acetone sensor.* ACS applied materials & interfaces, 2014. **6**(17): p. 14779-14784.
11. Murphy, A., et al., *Efficiency of solar water splitting using semiconductor electrodes.* International journal of hydrogen energy, 2006. **31**(14): p. 1999-2017.
12. Tamirat, A.G., et al., *Using hematite for photoelectrochemical water splitting: a review of current progress and challenges.* Nanoscale Horizons, 2016. **1**(4): p. 243-267.
13. Sivula, K., F. Le Formal, and M. Grätzel, *Solar water splitting: progress using hematite (α-Fe2O3) photoelectrodes.* ChemSusChem, 2011. **4**(4): p. 432-449.

14. Garg, A. and E. Matijević, *Preparation and properties of uniform coated inorganic colloidal particles: III. Zirconium hydrous oxide on hematite.* Journal of colloid and interface science, 1988. **126**(1): p. 243-250.
15. Luo, Z., et al., *Dendritic hematite nanoarray photoanode modified with a conformal titanium dioxide interlayer for effective charge collection.* Angewandte Chemie International Edition, 2017. **56**(42): p. 12878-12882.
16. Steier, L., et al., *Understanding the role of underlayers and overlayers in thin film hematite photoanodes.* Advanced Functional Materials, 2014. **24**(48): p. 7681-7688.
17. Subramanian, A., et al., *Trade-off between Zr passivation and Sn doping on hematite nanorod photoanodes for efficient solar water oxidation: effects of a ZrO2 underlayer and FTO deformation.* ACS Applied Materials & Interfaces, 2016. **8**(30): p. 19428-19437.
18. Wang, D., et al., *Enhanced photoelectrochemical water splitting on hematite thin film with layer-by-layer deposited ultrathin TiO2 underlayer.* International journal of hydrogen energy, 2014. **39**(28): p. 16212-16219.
19. Lian, S., et al., *Synthesis of magnetite nanorods and porous hematite nanorods.* Solid State Communications, 2004. **129**(8): p. 485-490.
20. Arzaee, N.A., et al., *Aerosol-assisted chemical vapour deposition of α-Fe2O3 nanoflowers for photoelectrochemical water splitting.* Ceramics International, 2019. **45**(14): p. 16797-16802.
21. Suresh, R., et al., *Facile synthesis of cobalt doped hematite nanospheres: magnetic and their electrochemical sensing properties.* Materials Chemistry and Physics, 2012. **134**(2-3): p. 590-596.
22. Li, C., et al., *Surviving High-Temperature Calcination: ZrO2-Induced Hematite Nanotubes for Photoelectrochemical Water Oxidation.* Angewandte Chemie, 2017. **129**(15): p. 4214-4219.
23. Quitério, P., et al., *Photoelectrochemical water splitting: thermal annealing challenges on hematite nanowires.* The Journal of Physical Chemistry C, 2020. **124**(24): p. 12897-12911.
24. Liu, J., et al., *Ge-doped hematite nanosheets with tunable doping level, structure and improved photoelectrochemical performance.* Nano Energy, 2013. **2**(3): p. 328-336.
25. Chaudhari, K.N., N.K. Chaudhari, and J.-S. Yu, *Peroxidase mimic activity of hematite iron oxides (α-Fe 2 O 3) with different nanostructures.* Catalysis Science & Technology, 2012. **2**(1): p. 119-124.
26. Li, M., et al., *Shape-controlled synthesis of magnetic iron oxide@ SiO2–Au@ C particles with core–shell nanostructures.* Langmuir, 2015. **31**(18): p. 5190-5197.
27. Phuan, Y.W., et al., *Prospects of electrochemically synthesized hematite photoanodes for photoelectrochemical water splitting: a review.* Journal of Photochemistry and Photobiology C: Photochemistry Reviews, 2017. **33**: p. 54-82.
28. Zhu, M., et al., *Hydrothermal synthesis of hematite nanoparticles and their electrochemical properties.* The Journal of Physical Chemistry C, 2012. **116**(30): p. 16276-16285.
29. Gajda-Schrantz, K., et al., *Formation of an electron hole doped film in the α-Fe 2 O 3 photoanode upon electrochemical oxidation.* Physical Chemistry Chemical Physics, 2013. **15**(5): p. 1443-1451.
30. Krysa, J., et al., *TiO2 and Fe2O3 films for photoelectrochemical water splitting.* Molecules, 2015. **20**(1): p. 1046-1058.
31. Nyarige, J.S., T.P. Krüger, and M. Diale, *Structural and optical properties of hematite and L-arginine/hematite nanostructures prepared by thermal spray pyrolysis.* Surfaces and Interfaces, 2020. **18**: p. 100394.

32. Fitzmorris, B.C., et al., *Ultrafast transient absorption studies of hematite nanoparticles: the effect of particle shape on exciton dynamics.* ChemSusChem, 2013. **6**(10): p. 1907-1914.
33. Malviya, K.D., et al., *Rigorous substrate cleaning process for reproducible thin □ lm hematite (a-Fe2O3) photoanodes.* J. Mater. Res, 2015: p. 2.
34. Liu, J., et al., *Highly oriented Ge-doped hematite nanosheet arrays for photoelectrochemical water oxidation.* Nano Energy, 2014. **9**: p. 282-290.
35. Guo, X., et al., *Synthesis and microwave absorption of uniform hematite nanoparticles and their core-shell mesoporous silica nanocomposites.* Journal of Materials Chemistry, 2009. **19**(37): p. 6706-6712.
36. Gaviria, J., et al., *Hematite to magnetite reduction monitored by Mössbauer spectroscopy and X-ray diffraction.* Physica B: Condensed Matter, 2007. **389**(1): p. 198-201.
37. Lagoeiro, L., *Transformation of magnetite to hematite and its influence on the dissolution of iron oxide minerals.* Journal of Metamorphic Geology, 1998. **16**(3): p. 415-423.
38. Zhu, W., et al., *Monodisperse porous pod-like hematite: hydrothermal formation, optical absorbance, and magnetic properties.* Materials Letters, 2011. **65**(6): p. 1003-1006.
39. Katsuki, H., et al., *Ultrafast microwave-hydrothermal synthesis of hexagonal plates of hematite.* Materials Chemistry and Physics, 2018. **205**: p. 210-216.
40. Nyarige, J.S., T.P. Krüger, and M. Diale, *Effects of L-arginine concentration on hematite nanostructures synthesized by spray pyrolysis and chemical bath deposition.* Physica B: Condensed Matter, 2020. **581**: p. 411924.
41. Caudron, E., et al., *Identification of hematite particles in sealed glass containers for pharmaceutical uses by Raman microspectroscopy.* Journal of pharmaceutical and biomedical analysis, 2011. **54**(4): p. 866-868.
42. Varshney, D. and A. Yogi, *Structural and electrical conductivity of Mn doped hematite (α-Fe2O3) phase.* Journal of Molecular Structure, 2011. **995**(1-3): p. 157-162.
43. Hamdi, M., Posva, F. and Grundler, D., *Spin wave dispersion of ultra-low damping hematite (α− Fe 2 O 3) at GHz frequencies.* Physical Review Materials, 2023. **7**(5), p.054407.
44. El Kanj, A., Gomonay, O., Boventer, I., Bortolotti, P., Cros, V., Anane, A. and Lebrun, R., *Antiferromagnetic magnon spintronic based on nonreciprocal and nondegenerated ultra-fast spin-waves in the canted antiferromagnet α-Fe2O3.* Science Advances, 2023. **9**(32), p.eadh1601.
45. Wang, H., et al., *Long-distance coherent propagation of high-velocity antiferromagnetic spin waves.* Physical Review Letters, 2023. **130**(9), p.096701.